Title: Granular column collapse: Analysing the effects of gravity levels

Yucheng Li*	li@gut.rwth-aachen.de	Institute of Geotechnical and Underground Technology, RWTH Aachen University
Raul Fuentes	raul.fuentes@gut.rwth-aachen.de	Institute of Geotechnical and Underground Technology, RWTH Aachen University

* Corresponding author

Granular column collapse: Analysing the effects of gravity levels

Yucheng Li* and Raul Fuentes

Institute of Geomechanics and Underground Technology, RWTH Aachen University, 52074 Aachen, Germany

*Corresponding author at: Institute of Geotechnical and Underground Technology, RWTH Aachen University, 52074 Aachen, Germany. E-mail address: li@gut.rwth-aachen.de (Yucheng Li). ORCID: 0009-0001-7806-1415

ABSTRACT

In this study, we investigated the effect of gravity level on the collapse of granular column using the Smoothed Particle Hydrodynamics (SPH) method based on the Mohr-Coulomb model. After validating the model with existing experimental studies, a dimensional analysis of the system's scaling factors was performed to evaluate the influence of varying gravity levels. The results show that gravity significantly influences collapse dynamics, particularly in shortening the collapse time. To predict collapse time, we propose two models that account for varying gravity acceleration (g), both of which scale positively with $N^{-1/2}$ ($g = NG$, where N is the gravity scaling factor, $G = 9.81\text{m/s}^2$). We find that the non-dimensional collapse time, t_∞/τ_c (where t_∞ is the collapse time, and $\tau_c = \sqrt{h_0/g}$, with h_0 representing the initial height), is influenced by the initial aspect ratio, a (defined as $a = h_0/r_0$, where r_0 is initial radius of the column). While gravity does impact collapse dynamics, its effects on the deposit run-out distance and final height remain consistently scaled at 1.0 across varying gravity levels. Additionally, we propose a modified mobility angle, θ', to investigate the effect of gravity on flow mobility, which aligns with expected gravity scaling. Furthermore, our findings are supported by observations of natural landslides in the Solar System. A multiscale analysis reveals that the spreading range of collapse is contingent on the sample volume and initial potential energy as opposed to gravity. This study provides insights for in-depth investigations into the collapse mechanism of granular materials in planetary exploration.

Keywords: Granular column collapse, Gravity level, Aspect ratio, Smoothed Particle Hydrodynamics

MANUSCRIPT submitted to Computers and Geotechnics

Authors: Yucheng Li & Raul Fuentes

1 Introduction

The flow of granular materials is widely encountered in nature and industry, playing a crucial role in various scenarios, such as the design of slopes, snow and rock avalanche risk assessment, ore mining and transshipment, and the movement of grain in agriculture. In these applications, an in-depth understanding of the collapse mechanisms and characterisation of granular flows is essential for effective disaster prevention and risk management.

A traditional and simple test to understand the collapse behaviour of granular flow is the granular column collapse. Lube et al. (2004) and Lajeunesse et al. (2004) conducted seminal simple experiments. They filled a cylindrical column with granular materials and allowed them to spread over a horizontal surface under gravity. Their results revealed that the collapse characteristics (e.g., flow pattern, run-out distance, and final height) are mainly, although not uniquely, governed by initial aspect ratio, *a*. Depending on the value of initial aspect ratio, two distinct regimes can be distinguished in terms of the run-out distance. When *a* is low, the flow exhibits a regime dominated by friction. In this regime, the column's edges fall while leaving its inner part relatively undisturbed. Notably, during this stage, a simple linear relation between the deposit run-out distance and the initial aspect ratio is commonly reported (Lube et al., 2004, Lajeunesse et al., 2004, Szewc, 2017). However, as *a* increases, the governing mechanism of granular flow changes. The shear plane gradually shifts inwards until the entire free surface collapse. The spreading of granular flow is influenced by the pressure gradient. In this regime, the deposit run-out distance follows a different relationship with aspect ratio, specifically a power law relationship. The final deposit for samples with low *a* exhibit a truncated cone shape in three dimensions (3D) or a trapezoid shape in two dimensions (2D), whereas models with high *a* trend to result in conical or triangular-shaped deposits. The effect of many other parameters have been investigated like initial column porosity (Fern and Soga, 2016), particle shape (Tapia-McClung and Zenit, 2012, Wei et al., 2018, Hoang and Nguyen, 2023), inter-particle friction (Lai et al., 2023), particle size (Lai et al., 2017, Cabrera and Estrada, 2021, Su et al., 2022), grain size effects (Warnett et al., 2014, Cabrera and Estrada, 2019, Man et al., 2021b), cohesive materials collapse (Jing et al., 2018a, Zhu et al., 2022), collapse in water (Thompson and Huppert, 2007, Jing et al., 2018b, Polanía et al., 2022). Investigations have also been conducted to analysis the effect of boundary geometry parameters, such as an erodible surface (Crosta et al., 2009, Mangeney et al., 2010), air fluidization (Roche et al., 2011), lateral wall width (Zhang et al., 2021), cross-section shape (Teng Man, 2022) or basal friction ((Li et al., 2024) of the granular column collapse. Although they have an influence on some of the characteristics and kinematics of granular collapse, the aspect ratio remains the dominating factor.

As space exploration advances, the prospect of utilizing resources from other planets and human colonisation is becoming increasingly viable. Humanity's understanding of outer planets is poised to expand significantly with ongoing national space programs, including National Aeronautics and Space

Administration (NASA) ’s Artemis program, which aims to return to the moon and send astronauts to Mars. On 15 May 2021, China’s Zhu Rong rover successfully landed on Mars, making China as the second country to operate a Mars rover. Through these endeavours, humanity has deepened its understanding of space and the origins of planets. In terms of research, understanding the properties of granular material (e.g., angle of repose, collapse behaviour) under varying gravity levels is crucial for space exploration. Several studies have investigated the dependence of the dynamic angle of repose on gravity; however, no broad consensus exists. While P. G. Hofmeister (2009) and Kleinhans et al. (2011) demonstrated a dependence on gravity, Nakashima et al. (2011) and Atwood-Stone and McEwen (2013) found no such relationship. The controversy was addressed by Marshall et al. (2018), whose classical passive Earth pressure experiments conducted during reduced gravity flights showed that the angle of repose is independence of gravity. Inspired by these previous studies on the angle of repose tests, we focus on the collapse behaviour of granular materials. The first models for granular flows in centrifuge systems were based on granular flow in a rotating drum (Arndt et al., 2006). Recent research has expanded these flow configurations to include sliding down on curved channels (Bowman et al., 2010, Gue. et al., 2010) and studying the flow rate during the discharge of a silo (Dorbolo et al., 2013). Cabrera and Wu (2017) investigated the dynamic of granular flows under centrifugal acceleration, revealing that as the slope angle and equivalent centrifuge acceleration increase, the flow velocity increase and flow height decreases asymptotically until a constant height. Compared to experimental studies, numerical simulations offer a more economical and accessible approach for investigating the effect of varying gravity levels. Cabrera et al. (2020) investigated the scaling principles for granular flow in a centrifugal acceleration field using discrete element method (DEM). Results show that granular flows scale consistently only when the Coriolis acceleration is negligible, and are severely altered otherwise.

To our knowledge, there is no study that has systematically explored the effect of gravity levels on granular column collapse. Consequently, the objective of the paper is to analyse the effects of varying gravity levels on the collapse of gravity-driven particle column. After validating our model against existing experimental studies, we conduct a comprehensive analysis of the scaling relationship between gravity levels and collapse responses. By comparing our simulations results with natural landslides in the Solar System, ranging from laboratory to large-scale scenarios, we establish a regression line that supports our conclusions.

This work is structured as follows: Section 1 introduces the SPH theory and outlines the model set-up, followed by the validation of the SPH model using experiments data from the literature. Section 2 presents the results regarding the influence of gravity levels on deposit profiles. This includes the flow patterns, scaling laws for collapse time, deposit run-out distance & final height, and flow mobility. Section 3 delves into the reasons of gravity effect on the collapse range. The final section comprises the conclusions of this paper.

1.1 SPH framework for the simulation of granular flow

Due to the mesh-free nature of the method and the continuous media-based characteristics, the Smoothed Particle Hydrodynamics (SPH) method has been broadly demonstrated for the modelling of large deformation problems including granular column collapse (Chen and Qiu, 2012, Szewc, 2017, Fávero and Borja, 2018, Kermani and Qiu, 2018, Yang et al., 2020, Bui and Nguyen, 2021). In SPH, a continuum domain is discretised into an assembly of particles, each of which possesses field variables (such as velocity and stress) and moves with its own velocity. The field variables are then calculated through a kernel approximation, as shown in Fig. 1. The equations are presented using the Einstein convention, where α, β, and γ denote the Cartesian coordinates.

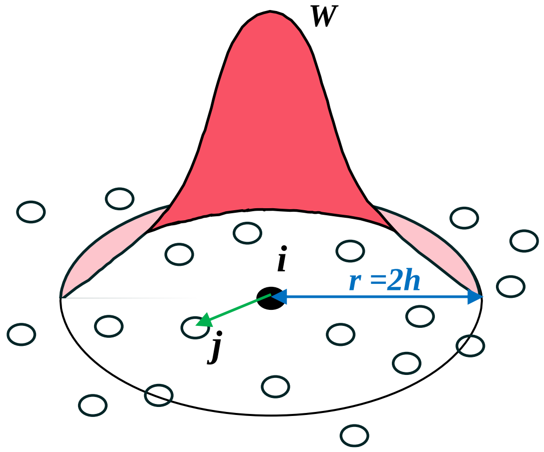

Fig. 1. Smoothing kernel function $W(\boldsymbol{x}, h)$ for particle i

The integral approximation of spatial function $f(\boldsymbol{x})$ at the point $\boldsymbol{x}$ is defined as,

$$\langle f(\boldsymbol{x})\rangle = \int_{\Omega} f(\boldsymbol{x}')W(\boldsymbol{x}-\boldsymbol{x}', h)d\boldsymbol{x}', \tag{1}$$

where Ω is the interpolation region, f is a function of the location vector $\boldsymbol{x}$ of the particle, and d$\boldsymbol{x}$ is a volume. W $(\boldsymbol{x}, h)$ is kernel function, where h is the smoothing length.

The discrete form of Eq. (1) can be written as,

$$\langle \nabla \cdot f(\boldsymbol{x})\rangle = \int_{\Omega} [\nabla \cdot f(\boldsymbol{x}')]W(\boldsymbol{x}-\boldsymbol{x}', h)d\boldsymbol{x}', \tag{2}$$

$W(\boldsymbol{x}, h)$ is defined using the function θ though the relation,

$$W(\boldsymbol{x}, h) = \frac{1}{h(x)^d}\theta(q), \tag{3}$$

where d is the number of space dimensions, and q is the relative distance, $q = |\boldsymbol{x}-\boldsymbol{x}'|/h$. $\theta(q)$ is the most commonly function cubic B-spline function and defined as,

$$\theta(q) = C\begin{cases} 1-\frac{3}{2}q^2+\frac{3}{4}q^3, & 0\le q\le 1 \\ \frac{1}{4}(2-q)^3, & 1\le q\le 2 \\ 0, & otherwise \end{cases}, \tag{4}$$

where C is a constant of normalization that depends on the number of the space dimensions.

Converting integral representations (as given in Eqs. (1) and (2)) into a particle approximation form:

$$\langle f(\boldsymbol{x_i})\rangle = \sum_{j=1}^{N}\frac{m_j}{\rho_j}f(\boldsymbol{x_j})W(\boldsymbol{x_i}-\boldsymbol{x_j},h), \tag{5}$$

$$\langle \nabla\cdot f(\boldsymbol{x_i})\rangle = \sum_{j=1}^{N}\frac{m_j}{\rho_j}f(\boldsymbol{x_j})\nabla\cdot W(\boldsymbol{x_i}-\boldsymbol{x_j},h), \tag{6}$$

where m_j is the mass of particle j, ρ_j is the density of particle j.

The general governing equations of mass and momentum conservation can be applied to granular material collapse as follows:

$$\frac{D\rho}{Dt} = -\rho\frac{\partial v^\alpha}{\partial x^\alpha}, \tag{7}$$

$$\frac{Dv^\alpha}{Dt} = \frac{1}{\rho}\frac{\partial\sigma^{\alpha\beta}}{\partial x^\beta}+b^\alpha, \tag{8}$$

where ρ is the material density; v^α is the velocity component; $\sigma^{\alpha\beta}$ is the stress tensor component; b^α is the acceleration due to the external forces.

The SPH approximation of governing equations can be derived using Eqs. (7) and (8). Writing partial differential governing equations in a discrete form. The mass conservation and momentum conservation in the framework of standard SPH becomes,

$$\frac{D\rho_i}{Dt} = \sum_{j=1}^{N}m_j\left(v_i^\alpha - v_j^\alpha\right)\frac{\partial W_{ij}}{\partial x_i^\alpha}, \tag{9}$$

$$\frac{Dv_i^\alpha}{Dt} = \frac{1}{\rho_i}\sum_{j=1}^{N}\frac{m_j}{\rho_j}\left(\sigma_i^{\alpha\beta}+\sigma_j^{\alpha\beta}\right)\frac{\partial W_{ij}}{\partial x_i^\beta}+b_i^\alpha, \tag{10}$$

where b_i^α is the force per unit mass due to gravitation. The Monaghan's type artificial viscosity is also implemented and shown in Appendix I.

To simulate the behaviour of the granular media we use a simple Mohr-Coulomb constitutive model where the yield surface and its plastic potential function are expressed as follows, respectively:

$$f = \sin\varphi I_1 + \frac{1}{2}\left[3(1-\sin\varphi)\sin\theta+\sqrt{3}(3+\sin\varphi)\cos\theta\right]\sqrt{J_2}-3c\cos\varphi = 0, \tag{11}$$

$$g = \sin\psi I_1 + \frac{1}{2}\left[3(1-\sin\psi)\sin\theta+\sqrt{3}(3+\sin\psi)\cos\theta\right]\sqrt{J_2}-3c\cos\psi, \tag{12}$$

where φ and ψ are the soil internal friction and dilatant angles, respectively; I_1, J_2, and J_2 are the first principal, second, and third deviatoric stress invariants, respectively; c is cohesion; and θ is the Lode angle, $\theta = \frac{1}{3}\cos^{-1}(1.5\sqrt{3}\,\frac{J_3}{J_2^{1.5}})$.

The general form of the elastic-perfectly plastic model is shown in Appendix. II.

To maintain the objectivity constitutive model under large deformation, the Jaumann stress tensor is adopted. The final form of the stress-strain relation for Mohr-Coulomb elastic-perfectly plastic constitutive model can be expressed by:

$$\dot{\sigma}^{\alpha\beta} = \sigma^{\alpha\gamma}\dot{\omega}^{\beta\gamma} + \sigma^{\gamma\beta}\dot{\omega}^{\alpha\gamma} + 2G\dot{e}^{\alpha\beta} + K\dot{\varepsilon}^{\gamma\gamma}\delta^{\alpha\beta} - \dot{\lambda}\Big[3K\sin\varphi\,\delta^{\alpha\beta} + 2G\big(\frac{\partial g}{\partial J_2}s^{\alpha\beta} + \frac{\partial g}{\partial J_3}t^{\alpha\beta}\big)\Big], \tag{13}$$

where $\dot{\varepsilon}^{\alpha\beta}$ and $\dot{\omega}^{\alpha\beta}$ are the strain and spin rate tensors, which can be related to the gradient of the velocity as follows:

$$\dot{\varepsilon}^{\alpha\beta} = \frac{1}{2}\left(\frac{\partial v^{\alpha}}{\partial x^{\beta}} + \frac{\partial v^{\beta}}{\partial x^{\alpha}}\right), \tag{14}$$

$$\dot{\omega}^{\alpha\beta} = \frac{1}{2}\left(\frac{\partial v^{\alpha}}{\partial x^{\beta}} - \frac{\partial v^{\beta}}{\partial x^{\alpha}}\right). \tag{15}$$

1.2 Model set-up

The dimensions of the granular column collapse model are shown in Fig. 2(a). It consists of a cylindrical domain placed over a rigid horizontal surface. The friction coefficient, μ, between the rigid plane and SPH particle was set to 0.4 in accordance with the validation experiments of Lube et al. (2004). Fig. 2 (b), (c), and (d) illustrate a sensitivity analysis of different particle spacings (Δp = 2.0, 3.0 or 5.0mm that represents the initial distance between adjacent particles) for an aspect ratio of 0.55. A red circle with a radius of 0.176 m was used as a standard reference size for better comparisons. Balancing computational cost and accuracy, the particle spacing, Δp = 3.0 mm was chosen for all simulations in this study.

The gravitational acceleration scaling factor, denoted as N (where $g = NG$, N=1/6, 1/3, 1, 2, and 10, G = 9.81m/s^2), is a crucial parameter in the simulation. Only the column height and gravitational acceleration were changed, while the column radius (r_0 = 0.1m) remained constant. The material density, angle of friction, Poisson’s ratio and Young’s modulus were 2600 $kg.m^{-3}$, 37°, 0.3, and 6.0 MPa respectively. A wide range of granular column aspect ratios are presented in Table 1.

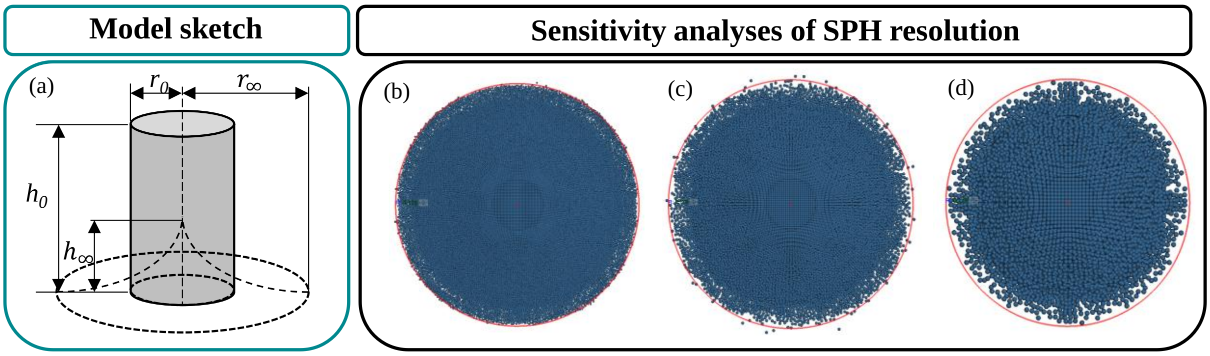

Fig. 2. (a) A sketch of the axisymmetric granular collapse: shaded region denotes the initial column (r_0: initial radius, h_0: initial height), dashed curve denotes deposit geometry (r_∞: final run-out distance, h_∞: final height). (b) Particle spacing (a = 0.55): Δp = 2.0mm & 220,080 SPH particles. (c) Δp = 3.0mm & 63,378 SPH particles. (d) Δp = 5.0mm & 13,904 SPH particles.

Table 1. Series of example granular column collapse.

Case ID	$a = h_0/r_0$	h_0 /m	No. of particles
1	0.55	0.055	63,378
2	1.0	0.10	119,714
3	1.5	0.15	176,050
4	2.75	0.275	323,932
5	4	0.4	471,814
6	6	0.6	704,200
7	10	1.0	1,176,014
8	13.8	1.38	1,619,660
9	18	1.8	2,112,600
10	25	2.5	2,932,993

1.3 Model validation

The numerical model was validated against the experiments of Lube et al. (2004) under the Earth's gravitation acceleration ($G = 9.81\text{m/s}^2$), focusing on three key aspects: deposit pattern, run-out distance, and final height. Figure. 3 presents deposit patterns of numerical simulations and experimental results. Depending on the aspect ratio values results, three distinctly different deposit patterns are shown. For small aspect ratios (e.g., a = 0.55), a flat surface remains at the top of the model; for intermediate aspect ratios (e.g., a = 2.75), the top surface changes from a flat plate to a conical tip; for large aspect ratios (e.g., a = 13.8), the sand forms an outward propagating wave during the process, transferring mass from the centre to the edge of the diffusion. Our numerical flow patterns agree well with the experimental results (Lube et al., 2004, Lajeunesse et al., 2004) and numerical results (Man et al., 2021a, Sheikh et al., 2021).

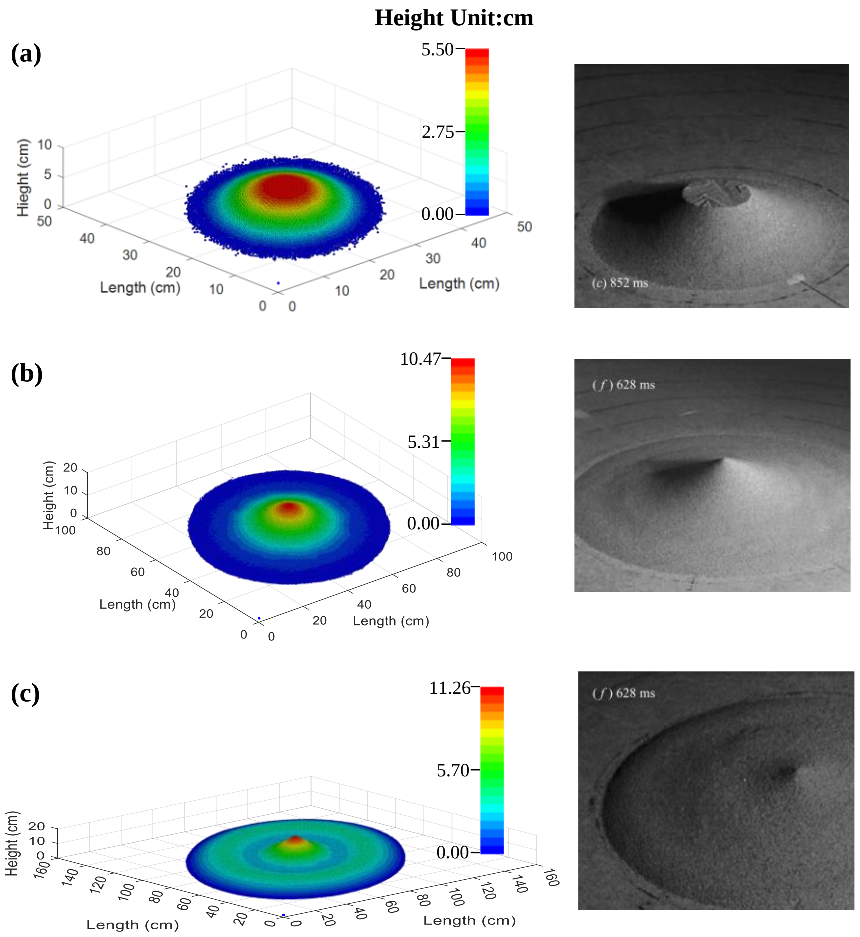

Fig. 3. Qualitative comparison of numerical (left images) and experimental results (right grey images) reported by Lube et al.2004 of deposit profiles at three typically aspect ratios. (a) *a* = 0.55. (b) *a* = 2.75. (c) *a* = 13.8.

Figure. 4(a) shows the validation of the run-out distance. Our simulation results against well the experimental points and formula form (see Eq. (16)) of Lube et al. (2004).

Our results of final height, h_∞, are plotted in Fig. 4(b) and are in good agreement with the experimental and formula (Eq. (17)) results. The critical aspect ratio also fits also well with the 1.0 proposed by Lube et al. (2004). When the aspect ratio is less than 1.0, the model shows circular truncated cones pattern. The model maintains the initial height (e.g., *a* = 0.55, Fig. 3). The morphology becomes more complex when the aspect ratio exceeds 1.0 (e.g., *a* = 2.75 or *a* = 13.8, Fig. 3).

$$\frac{r_\infty - r_0}{r_0} = r^* \simeq \begin{cases} 1.24a, & a < 1.7 \\ 1.6a^{1/2}, & a \geq 1.7 \end{cases} \tag{16}$$

$$\frac{h_\infty}{r_0} = h^* = \begin{cases} a, & 0 \leq a < 1.0 \\ 0.88a^{1/6}, & 1.0 \leq a < 10 \end{cases} \tag{17}$$

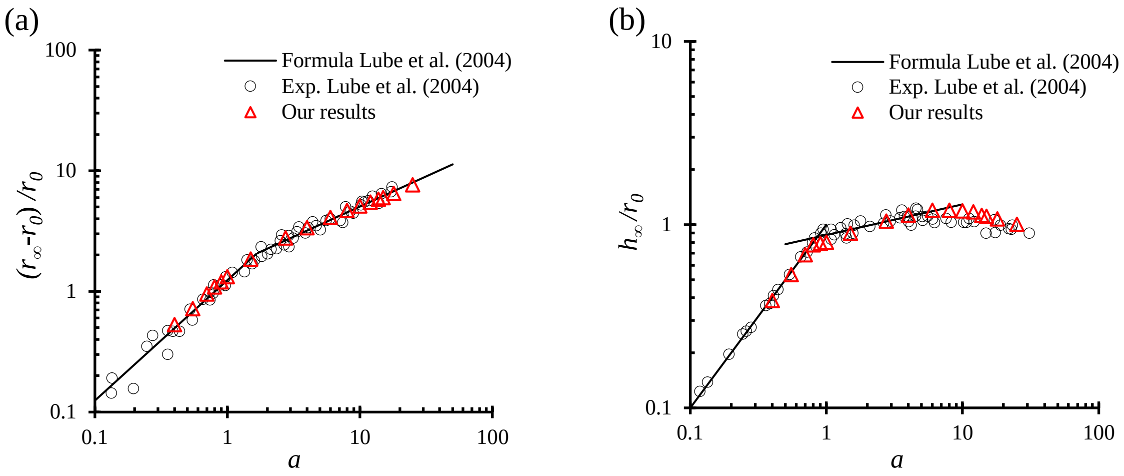

Fig. 4. The relationship between rescaled final height and initial aspect ratio. (a) run-out distance; (b) final height.

1.4 Assumption of scaling factors

Before analysing the results, we assume that the gravity level should obey certain scaling laws. To validate this assumption and extend it to other aspect ratios, and regimes, we conduct a scaling analysis of the problem, starting from a hypothesis that scaling derived from simple dimensional analysis is sufficient. The actual scaling factors of this hypothesis assume a scaling N of gravity and a scaling of 1.0 for density and length. This leads to the overall scaling factors shown in Table 2. In the following sections, we will compare these values with those in the literature and our obtained results.

Table 2. Scaling factors assuming a simple dimensional analysis. *Indicates enforced scaling parameters in the system.

Variable	*Units*	*Scaling values*
*L**	*m*	*1*
*ρ**	*kg/m3*	*1*
*g**	*m/s2*	*N*
F	*N*	*N*
Stress	*N/m2*	*N*
v	*m/s*	$N^{1/2}$
t	*s*	$N^{-1/2}$
Energy	*J*	*N*

2 Results

2.1 *Typical evolution of avalanche flow patterns*

In Fig. 5, a typical aspect ratio (e.g., a = 4) was used to demonstrate the effect of gravity levels on the evolution of flow patterns. As expected, higher gravity levels accelerate the collapse process. This is consistent with the conclusion of Meruane et al. (2010), who claimed that the flow velocity and duration of emplacement are gravity dependent. Additionally, we initially find that the varying gravity levels produce same deposit morphologies (bottom row of Fig. 5). This indicates that the gravity has a significant influence on the dynamics of the collapse of granular column but no impact on the deposit morphology.

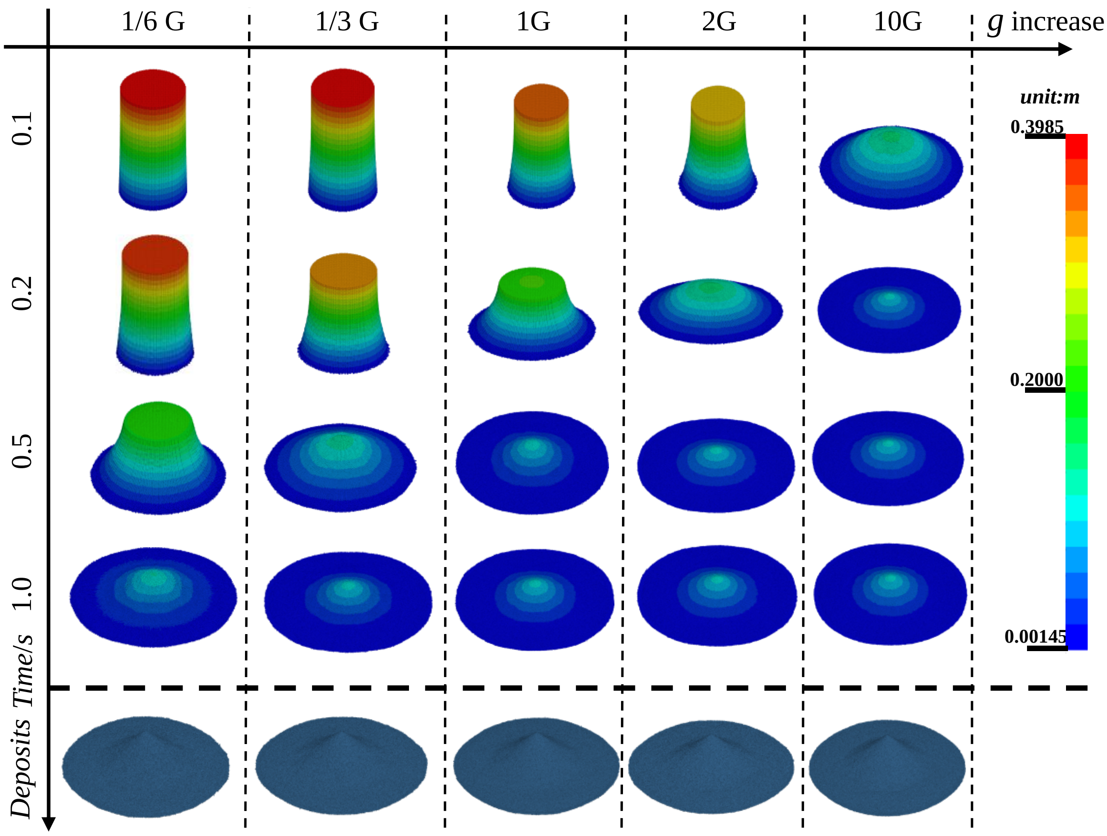

Fig. 5. Snapshots of granular column collapse at different gravity levels. The bottom blue pictures are final deposit morphologies.

2.2 *Collapse time prediction models*

2.2.1 *Scaling by the initial geometry*

The relationship between scaling factor (N) of varying gravity and the collapse time of granular column was investigated. Lube et al. (2004) investigated scenarios with the same gravitational acceleration (g)

but different initial radius (r_0 = 2.9, 7.5, and 9.7cm). Their findings indicated that different r_0 has no effect on the non-dimensional collapse time.

$$\frac{t_\infty}{\sqrt{r_0/g}} = f(a) \tag{18}$$

In this work, we keep r_0 constant while varying gravity levels to examine the effect of gravity on the collapse dynamics. Fig. 6 shows the non-dimensional collapse time and the scaling laws derived from our results. Our new correlation is shown in Eq. (19) with a value of R^2 = 0.995. This scaling by $1/\sqrt{g}$ aligns with the observations of Lube et al. (2004) and their developed Eq. (18). Both our results and experimental of Lube et al. (2004) show an increasing trend in non-dimensional time as the aspect ratio increases. We observe a deviation for values of a larger than 5.0. The fit is satisfactory for a < 5.0, with discrepancies only present in scenarios with larger aspect ratios. This reason for this bias may be that they had insufficient data with larger aspect ratios in their experiments (their fitting form was mainly based on a < 5.0, with only 5 tests between 5.0 < a < 15.0, and no cases with a >15.0).

$$\frac{t_\infty}{\sqrt{r_0/g}} = 3.776 * a^{0.35} \tag{19}$$

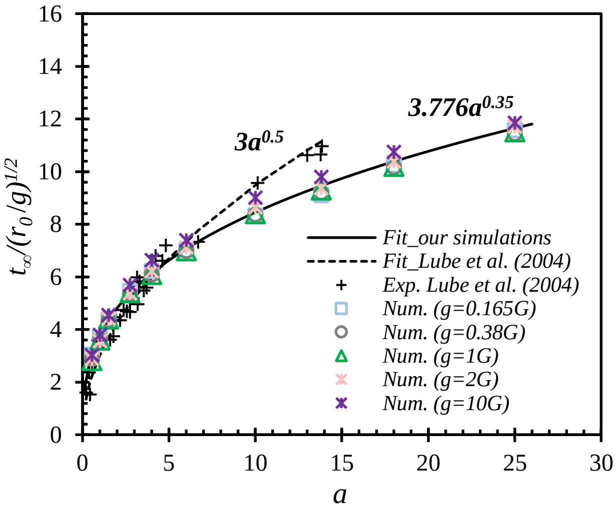

Fig. 6. The scaling laws of collapse time and the scaling laws obtained from regression analysis for different gravity levels.

2.2.2 *Scaling by the characteristic time*

Another approach for predicting collapse time was used based on the analysis of single-particle free fall, where $h = \frac{1}{2}gt^2$, then $t = \sqrt{2h/g}$. Here, by introducing the characteristic time scale τ_c ($\tau_c = \sqrt{h_0/g}$) to evaluate the collapse time, we derive Eq. (20) with R^2=0.97, and illustrate the fitted results in Fig. 7.

$$\frac{t_\infty}{\tau_c} = \frac{3.712}{a^{0.14}} \tag{20}$$

Lajeunesse et al. (2005) claimed that the propagation evolution can be differentiated into three sections. In the first section ($t < 0.8\tau_c$) the collapse process accelerates, resulting in the spreading of the deposit tip in a positive horizontal direction. Subsequently, the foot of the material propagates at nearly constant velocity for about $2\tau_c$. In the final section, the material propagation decreases until it reaches the final deposit position after approximately $0.6\tau_c$. They define approximately $3\tau_c$ as a guide value for the total duration of the collapse. However, our results show that the non-dimensional collapse time (t_∞/τ_c) is not a constant value, but it is also affected by the initial aspect ratio. Specifically, at lower aspect ratios (a < 5.0), the non-dimensional collapse time tends to decrease rapidly, and this trend diminishes as the aspect ratio increases. Based on Eq. (20), we calculated that the ratio of the collapse time to the free-fall time ($t_\infty/\sqrt{2\,h_0/g}$) of a single particle decreases as the aspect ratio increases (see the black dashed line in Fig. 7). This finding differs from that of Lube et al. (2004), who reported that the collapse time of granular materials in columns is approximately twice the free fall time (see the red dashed line in Fig. 7). The discrepancy may lie in the higher columns, whose collapse mechanism is predominantly influenced by pressure gradients, resulting in a short collapse time that tends to a free-fall state.

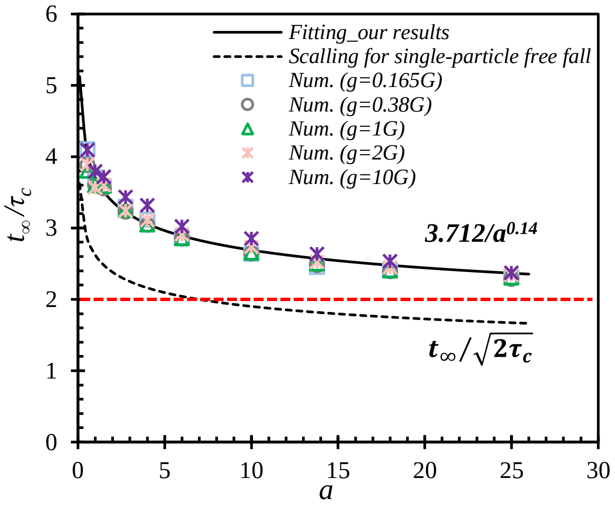

Fig. 7. Influence of gravity level on the collapse time normalized by the characteristic time. The black dashed line is the scaling line for single-particle free fall condition ($t_\infty/\sqrt{2\tau_c}$) derived from the regression analysis of simulation results (black line).

Eq. (19) or Eq. (20) can be easily compared. In both equations, the collapse time is positively correlated with $1/\sqrt{g}$, represented as $N^{-1/2}$, agreeing with previous studies that assumed scaling factors in Table 2. This suggests that we can use Eq. (19) or Eq. (20) to estimate the collapse time at different gravity levels, once knowing the necessary parameters.

2.3 *Deposit run-out distance*

Fig. 8 presents the correlation between run-out distance and aspect ratio at different gravity levels. The expected scaling of 1.0 (see Table 2) is clearly confirmed for the numerical results, indicating that the gravity level does not impact the normalized run-out distance. Moreover, the gravity level does not alter the critical aspect ratio at which the shift occurs in the bilinear relationship shown in Fig. 8. It remains a constant value at 1.7, as noted in Eq. (16).

Additionally, large-scale results, such as the natural landslides in Solar System (Lucas et al., 2014), present a regression line with a slope of 12.64 and R^2=0.88. Notably, the landslides on Mars and Iapetus also align well with this regression line, supporting our conclusion about the consistent effect of gravity on run-out distance across different celestial bodies. This finding is also consistent with the work of Roche et al. (2011), who normalized the run-out distance of the Valles Marineras (Lajeunesse et al., 2006, Lucas et al., 2011), delimited by blue dashed lines with slopes of 3.3 and 11.5 (see blue arbitrary lines in Fig. 8). While their results indicate a larger value compared to both our simulations and granular column experimental findings, it confirms the scaling. The differences in magnitude can be explained by the fact that natural landslides travel unexpectedly long distances, indicating lower dissipation during collapse, potentially induced by other mechanisms such as material entrainment or water lubrication. However, the precise physical processes underlying energy dissipation during natural granular flows remain uncertain (Lucas et al., 2014).

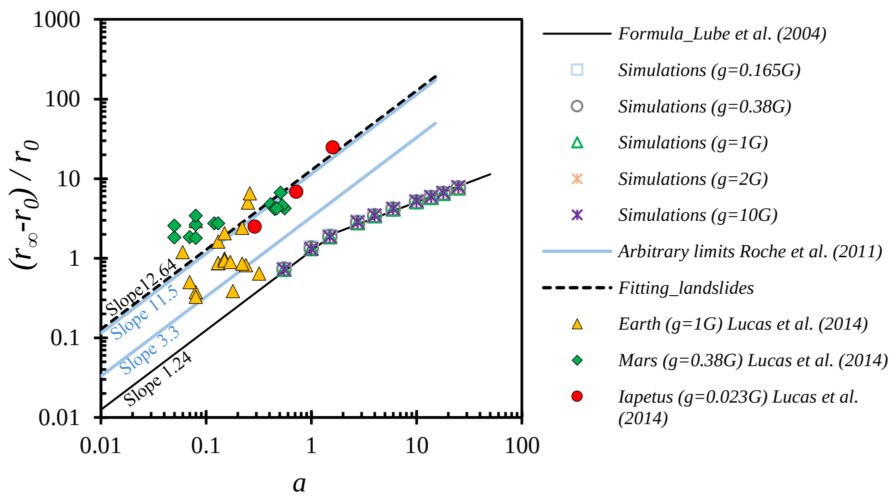

Fig. 8. Influence of gravity level on the normalized run-out distance. The natural data of landslides in Earth, Mars, and Iapetus are referenced from Lucas et al. (2014).

2.4 *Final height*

Fig. 9(a) presents the rescaled final height at various aspect ratios. Again, the expected scaling of 1.0 is consistently observed across different aspect ratio ranges. The results also align well with our proposed formula for final height when a > 10 (as indicated by the blue and red lines in the inset of Fig. 9(a)), with some nuances at high aspect ratios. To further analysis these differences in detail, we conducted a cross-sectional of deposit profiles for a = 25 (see Fig. 9(b)). The deposit morphology appears very similar, as depicted in the inset of Fig. 9(b). Notably, we observed a slightly lower final height under high gravity conditions (e.g., g = 10G), although the effect was negligible.

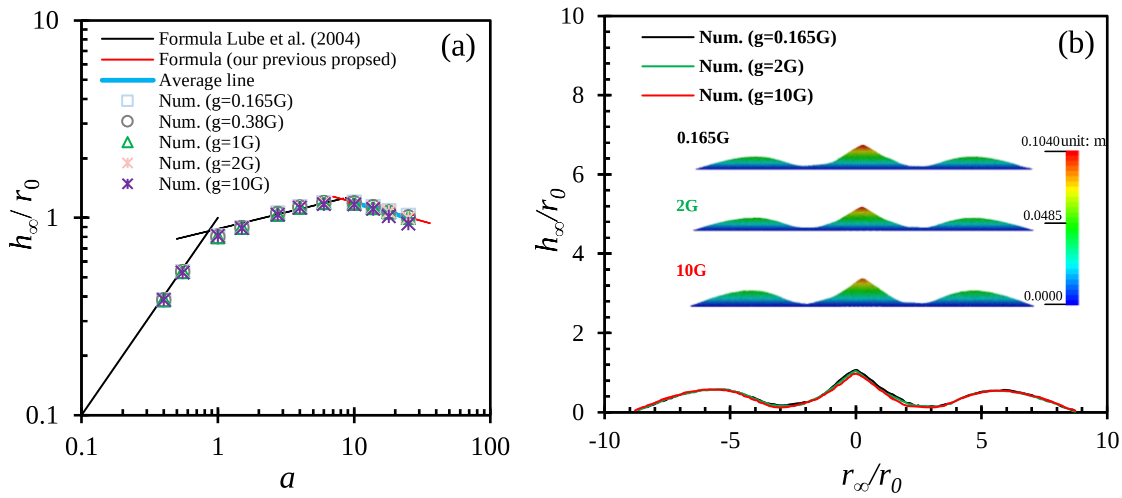

Fig. 9. (a) The rescaled final height versus aspect ratio at different gravity conditions. (b) Deposit profiles $f(r, h)$ normalized to the column radius. The deposit cross-section profiles of a=25 (height coordinates) at different gravity levels (0.165G, 2G, and 10G) are presented in the inset.

2.5 Flow mobility

The particles in dry granular flow under the driving force of gravity. It is very important to quantitatively analysis the effect of gravity levels on the flow mobility. The reciprocal of the granular flow mobility can be measured by the ratio of h_∞ and r_∞ (Cagnoli and Piersanti, 2015, Lai et al., 2017) in Eq. (21). The angle θ is referred to as the flow mobility angle (see the inset of Fig. 10). The higher the flow mobility of the flow, the smaller the angle. We introduced another mobility angle, θ', in Eq. (22) where we normalise by the initial column radius. The angle is referred to as the modified flow mobility angle (see the inset of Fig. 10).

$$tan\theta = h_\infty / r_\infty \tag{21}$$

$$tan\theta' = h_\infty / (r_\infty - r_0) = h^* / r^* \tag{22}$$

It was observed that both θ and θ' decreases as the aspect ratio increases, following the expected scaling with the gravity level. However, θ exhibits a small peak point at $a \approx 1$, which is attributed to the effect of initial geometry. A straightforward validation, as depicted in the inset of Fig. 10(b), illustrates that when a < 0.8, the model, dominated by friction, maintains the initial height h_0. As a increases, h_0 increases more rapidly than r_∞, leading to an increasing trend for θ. Only when $a \geq 0.8$, h_∞ decreases with r_∞, resulting in a lower θ. Conversely, θ' eliminates the effect of the initial geometry (r_0), and the curve undergoes continuous variation. As the aspect ratio increases, the initial geometry effect diminishes, eventually causing θ' to approach θ.

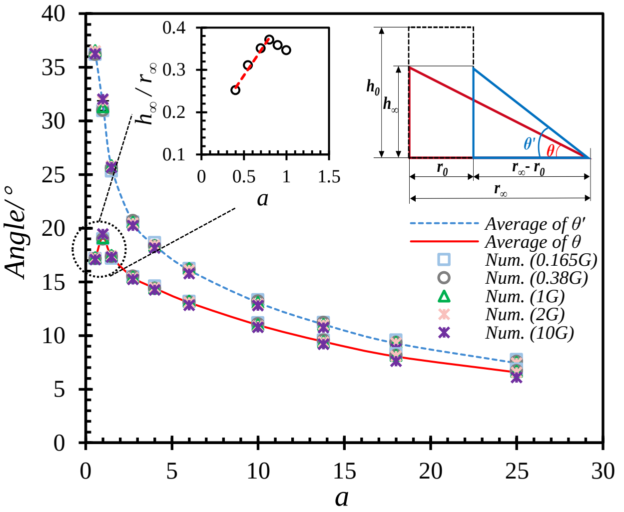

Fig. 10. The effect of gravity levels on the flow mobility. The sketch of mobility angle θ and θ' are shown in the inset. The inset also shows the validation results for model at $\mu = 0.4$ and g = 1G.

3 Discussion

Comparing experimental or simulation results with actual engineering data is essential for validating and refining the model, as well as for understanding its applicability in real-word scenarios. As depicted in Fig. 8, the aspect ratio of natural landslides typically falls well below 1.0 and in a much narrower range compared to experiments. Consequently, using aspect ratio as a criterion for analysing the large-scale landslides may not be suitable. Motivated by this, we investigated the effect of gravity level on the relationship between the length travelled (ΔL) and landslide initial volume, as shown in Fig. 11. The results suggest that the run-out distance is independent of gravity level, which is consistent for small-scale and large-scale slides. Through regression analysis, a critical point in volume was identified, corresponding to $1.5 \leq a \leq 2.75$. This critical point closely corresponding to the transition point of 1.7 identified by Lube et al. (2004). For volumes less than this critical point, our simulation results, along with experimental findings (Warnett et al., 2014), exhibit a linear increasing trend as volume increases. Conversely, for volumes greater than this critical point, our small-scale results fit well with large-scale landslide data, showing a power increase trend. This finding is consistent with previous research by Lajeunesse et al. (2005), who suggested that in lower columns, collapse is primarily influenced by friction, while in higher columns, it is governed by pressure gradients. The existence of this critical point also reflects the transition phase between the influence of slide volume effects on the spreading distance at small and large scales.

The maximum kinetic energy (E_K) under different gravity level also scales well with a scaling factor of N, as shown in Fig. 12. That further supports that the gravity level does not influence the deposit run-out distance.

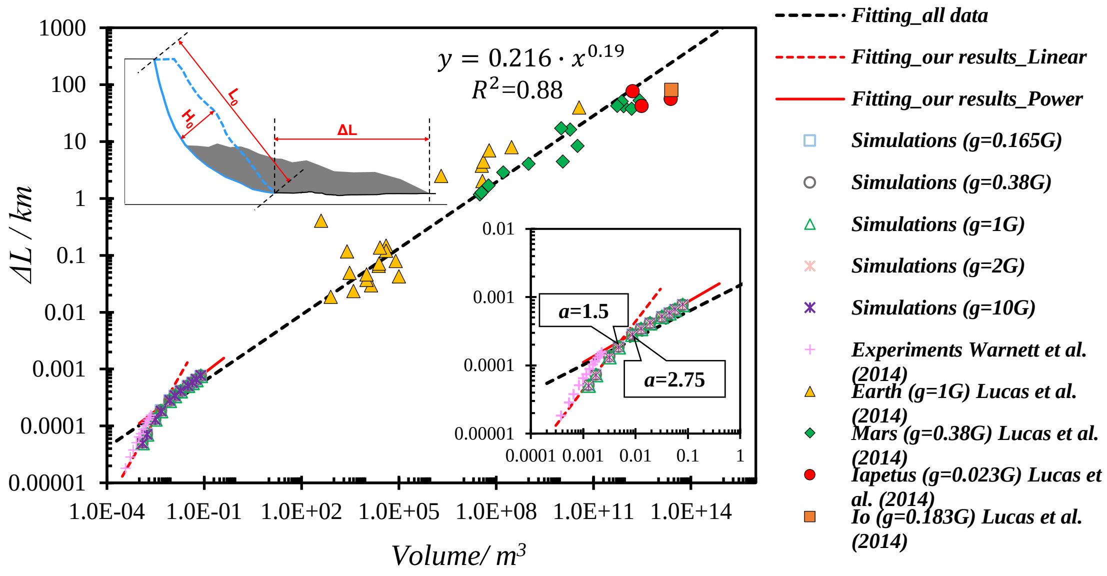

Fig. 11. The travel length (ΔL) as a function of initial volume. H_0 is the maximum initial thickness, L_0 the initial length and ΔL is the travel length by the front landslide. The inset figure illustrates the most frequent geometry for natural landslides, where the dashed blue region represents the initial geometry, and the grey region represents the deposit geometry. The volume corresponds to the aspect ratio point is depicted in the insert figure. The fitting formula for landslide data (Lucas et al., 2014) is also shown in the inset.

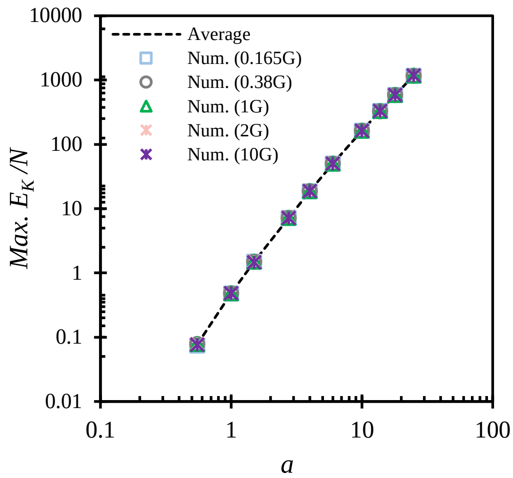

Fig. 12. The maximum of kinetic energy E_K scaled by a factor of N at different aspect ratios.

Strom et al. (2019) also analysed the dependency of run-out distance or affected area on the product of $V \times H_{max}$, which is a proxy to initial potential energy. We compared our small-scale simulation results and the experimental findings of Warnett et al. (2014) with large-scale landslide data from the Solar

System (Lucas et al., 2014), as shown in Fig. 13. We constructed a best-fit regression line (depicted as a black dashed line), achieving an R^2 value of 0.87. This highlights the consistency of small-scale results with large-scale landslide data, emphasizing the significance of potential energy as a crucial factor influencing deposit run-out distance.

Moreover, the obtained regression line validates that the gravity level scales according to our proposed model scaling. Additionally, the total potential energy of our simulations aligns well with a scaling factor N across different aspect ratios, as illustrated in the inset of Fig. 13.

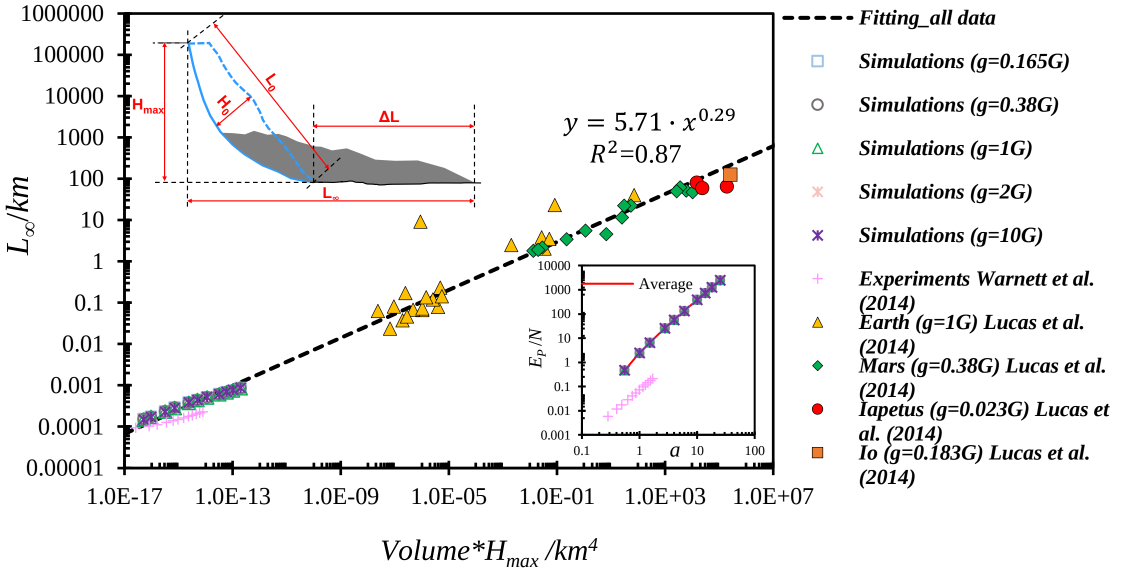

Fig. 13. Relationships between run-out distance and product of landslide volume and maximal height at different gravity conditions. H_{max} is the maximum elevation of the initial mass, H_0 is the maximum initial thickness and L_∞ is the total travel length of the landslide.

4 Conclusions

In this study, we use the Smoothed Particle Hydrodynamics (SPH) model and literature results to investigate the effects of gravity conditions on gravity-driven particle column collapse. This research explores how varying gravity levels influence collapse behaviours through a scaling analysis of non-dimensional collapse time, deposit geometry, and energy analysis. The results are summarized as follows:

(1) Higher gravity levels significantly shorten the collapse time of granular column while maintaining similar deposit morphologies. This suggests that gravity levels play a significant role in the dynamics of collapse but have no impact on the deposit morphology.

(2) To accurately predict the collapse time of granular column, two models were proposed, each accounting for different gravity levels. Both models demonstrate a positive correlation with $1/\sqrt{g}$,

represented as $N^{-1/2}$. We found that the non-dimensional collapse time (t_∞/τ_c) is not a constant but influenced by the initial aspect ratio. We also found that the ratio of the collapse time to the free-fall time ($t_\infty/\sqrt{2\,h_0/g}$) of a single particle decreases as the aspect ratio increases, eventually tends to a free-fall state.

(3) Gravity levels appear to have minimal effect on deposit run-out distance and final height. The expected scaling of 1.0 is clearly observed, suggesting that gravity level does not affect the normalized run-out distance. This conclusion aligns with observations of natural landslides in the Solar System over a large range of slide geometries. Moreover, the gravity level does not alter the critical aspect ratio (a = 1.7), where a shift occurs in the bilinear relationship. The rescaled final height remains consistent across various aspect ratio ranges, supported by cross-sectional analysis of deposit profiles for a = 25. Notably, only under high gravity condition (e.g., 10G) was a slight decrease in final height observed, although the effect was negligible and may be due to small numerical issues.

(4) Flow mobility was used to quantitatively describe the effect of gravity levels on deposit results. A modified mobility angle (θ') was proposed to eliminate the effect of the initial geometry (r_0). It was observed that both θ and θ' decreases as the aspect ratio increases, following the expected scaling of the gravity level. θ exhibits a small peak point at $a \approx 1$, which is attributed to the effect of initial geometry. Conversely, the curve of θ' undergoes continuous variation. As aspect ratio increases, the initial geometry effect diminishes, eventually causing θ' to approach θ.

(5) Through multiscale studies exploring the genesis of collapse geometry in terms of volume or height drop, we observed that small scale results (e.g., experiments) are in good agreement with large scale results (e.g., landslide). Notably, under identical scaling conditions (e.g., identical density, length, etc.), the extent of collapse appears to be independent of gravity level. Instead, it is found to depend on sample volume and initial potential energy. The sample volume factor exhibits a clear scale effect, with the critical point occurring at around a = 1.7. Furthermore, both gravitational potential and kinetic energies demonstrate a good scaling relationship with N, providing additional support for the conclusions drawn from an energy perspective.

CRediT authorship contribution statement

Yucheng Li: Conceptualization, Methodology, Validation, Investigation, Writing-original draft.

Raul Fuentes: Resources, Writing-review & editing, Supervision.

Declaration of Competing Interests

The authors declare that they have no known competing financial interests or personal relationships that could have appeared to influence the work reported in this paper.

Data availability

Data will be made available on request.

Acknowledgements

The first author would like to acknowledge the financial support provided by the China Scholarship Council for Doctoral Studies no.201808310302.

Appendix I: SPH artificial viscosity

The concept of artificial viscosity was first proposed in one spatial dimension by Ref. (VonNeumann and Richtmyer, 1950) to model flows with shocks, which is nowadays widely used in wave propagation programs. The role of the artificial viscosity is to smooth the shock over several particles. The artificial viscosity term Π_{ij} (Monaghan and Gingold, 1983) is included in the SPH momentum equation as:

$$\frac{Dv_i^\alpha}{Dt} = \sum_{j=1}^{N} m_j \left(\frac{\sigma_i^{\alpha\beta} + \sigma_j^{\alpha\beta}}{\rho_i \rho_j} + \Pi_{ij} \delta^{\alpha\beta} \right) \frac{\partial W_{ij}}{\partial x_i^\beta} + b_i^\alpha. \tag{23}$$

where **I** is the identity matrix. The most widely used form of artificial viscosity is:

$$\Pi_{ij} = \begin{cases} \dfrac{-\alpha c_{ij} \phi_{ij} + \beta \phi_{ij}^2}{\rho_{ij}}, & u_{ij} \cdot x_{ij} < 0 \\ 0, & u_{ij} \cdot x_{ij} \gg 0 \end{cases} \tag{24}$$

$$\phi_{ij} = \frac{h_{ij} \boldsymbol{v}_{ij} \cdot \boldsymbol{x}_{ij}}{\left| x_{ij}^2 \right| + 0.01 h_{ij}^2}, \; c_{ij} = \frac{c_i + c_j}{2}, \; \rho_{ij} = \frac{\rho_i + \rho_j}{2}, \tag{25}$$

$$h_{ij} = \frac{h_i + h_j}{2}, \boldsymbol{x}_{ij} = \boldsymbol{x}_i - \boldsymbol{x}_j, \boldsymbol{v}_{ij} = \boldsymbol{v}_i - \boldsymbol{v}_j, \tag{26}$$

where α and β are the problem dependent tuning parameters, and c is the sound speed. J.J.Monaghan (1994) chose $\alpha = 0.01$, $\beta = 0$ to simulate the free surface flow. Bui et al. (2007) chose $\alpha = 0.01$, $\beta = 1$ for water and $\alpha = 1$, $\beta = 1$ for soil. Here, $\alpha = 0.06$ and $\beta = 1.5$ are chosen based on numerical validation against the experimental study and direct comparison to J.J.Monaghan (1994) and Bui et al. (2007). The speed of sound c of the material is calculated according to $c_i = \sqrt{E_i/\rho_i}$. E is the Young's modulus of the material, assuming isotropic and homogeneous conditions.

Appendix. II: Generalized form of elastic-perfectly plastic model

Here, the general form of the elastic-perfectly plastic model is derived. The definition of total strain rate tensor, which can be divided into elastic and plastic parts, as follows:

$$\dot{\varepsilon}^{\alpha\beta} = \dot{\varepsilon}_e^{\alpha\beta} + \dot{\varepsilon}_p^{\alpha\beta}, \tag{27}$$

where the subscripts *e* and *p* present for elastic and plastic components, respectively.

The elastic strain rate tensor can be calculated by generalised Hooke's law:

$$\dot{\varepsilon}_e^{\alpha\beta} = \frac{\dot{s}^{\alpha\beta}}{2G} + \frac{1}{9K}\dot{\sigma}^{rr}\delta^{\alpha\beta}, \tag{28}$$

where $\dot{\varepsilon}^{\alpha\beta}$ is the deviatoric stress rate tensor; *G* and *K* are the material shear and bulk modulus; $\delta^{\alpha\beta}$ is the Kronecker's delta.

The plastic strain rate tensor can be derived from the plastic flow rule according to:

$$\dot{\varepsilon}_p^{\alpha\beta} = \dot{\lambda}\frac{\partial g}{\partial \sigma^{\alpha\beta}}, \tag{29}$$

where $\dot{\lambda}$ is the time rate of the plastic multiplier; g is the plastic potential function.

Substituting Eqs. (29) and (30) into Eq. (28) and rearranging the obtained equation, the generic form of the elastic-perfectly plastic is given by:

$$\dot{\sigma}^{\alpha\beta} = 2G\dot{e}^{\alpha\beta} + K\dot{\varepsilon}^{\gamma\gamma}\delta^{\alpha\beta} - \dot{\lambda}\left[\left(K - \frac{2G}{3}\right)\frac{\partial g}{\partial \sigma^{mm}}\delta^{mn}\delta^{\alpha\beta} + 2G\frac{\partial g}{\partial \sigma^{\alpha\beta}}\right], \tag{30}$$

where $\dot{e}^{\alpha\beta} = \dot{\varepsilon}^{\alpha\beta} - \frac{1}{3}\dot{\varepsilon}^{\gamma\gamma}\delta^{\alpha\beta}$ is the deviatoric strain rate tensor; *m* and *n* are free indexes, which are independent from α and β.

The plastic multiplier for the elastic-perfectly plastic model can be derived from the consistency condition, which requires the following:

$$df = \frac{\partial f}{\partial \sigma^{\alpha\beta}}d\sigma^{\alpha\beta} = 0, \tag{31}$$

where *f* is the yield function that defines the onset of plastic deformation.

Substituting Eq. (31) into Eq. (32), the general form of the time rate of the plastic multiplier can be obtained as,

$$\dot{\lambda} = \frac{\frac{\partial f}{\partial \sigma^{\alpha\beta}}\left[2G\dot{\varepsilon}^{\alpha\beta} + \left(K - \frac{2G}{3}\right)\dot{\varepsilon}^{\gamma\gamma}\delta^{\alpha\beta}\right]}{2G\frac{\partial f}{\partial \sigma^{mn}}\frac{\partial g}{\partial \sigma^{mn}} + \left(K - \frac{2G}{3}\right)\frac{\partial f}{\partial \sigma^{mn}}\delta^{mn}\frac{\partial g}{\partial \sigma^{mn}}\delta^{mn}}. \tag{32}$$

Substituting the Mohr-Coulomb yield function f and its plastic potential function g into Equation (32), the general form of the plastic multiplier reads the following:

$$\dot{\lambda} = \frac{1}{H}\left[3K\frac{\partial f}{\partial I_1}\dot{\varepsilon}^{\gamma\gamma} + 2G\left(\frac{\partial f}{\partial J_2}s^{\alpha\beta} + \frac{\partial f}{\partial J_3}t^{\alpha\beta}\right)\dot{\varepsilon}^{\alpha\beta}\right], \tag{33}$$

where H and $t^{\alpha\beta}$ are defined as follows:

$$H = 9K\frac{\partial f}{\partial I_1}\frac{\partial g}{\partial I_1} + 4GJ_2\frac{\partial f}{\partial J_2}\frac{\partial g}{\partial J_2} + 6GJ_3\left(\frac{\partial f}{\partial J_2}\frac{\partial g}{\partial J_3} + \frac{\partial g}{\partial J_2}\frac{\partial f}{\partial J_3}\right) + 2G\left(s^{\alpha m}s^{m\beta}s^{\alpha n}s^{n\beta} - \frac{4}{3}J_2^2\right)\frac{\partial f}{\partial J_3}\frac{\partial g}{\partial J_3}, \tag{34}$$

$$t^{\alpha\beta} = s^{\alpha m}s^{m\beta} - \frac{2}{3}J_2\delta^{\alpha\beta}. \tag{35}$$

References

ARNDT, T., BRUCKS, A., OTTINO, J. M. & LUEPTOW, R. M. 2006. Creeping granular motion under variable gravity levels. *Phys Rev E Stat Nonlin Soft Matter Phys,* 74**,** 031307.

ATWOOD‐STONE, C. & MCEWEN, A. S. 2013. Avalanche slope angles in low‐gravity environments from active Martian sand dunes. *Geophysical Research Letters,* 40**,** 2929-2934.

BOWMAN, E. T., LAUE, J., IMRE, B. & SPRINGMAN, S. M. 2010. Experimental modelling of debris flow behaviour using a geotechnical centrifuge. *Canadian Geotechnical Journal,* 47**,** 742-762.

BUI, H. H. & NGUYEN, G. D. 2021. Smoothed particle hydrodynamics (SPH) and its applications in geomechanics: From solid fracture to granular behaviour and multiphase flows in porous media. *Computers and Geotechnics,* 138.

BUI, H. H., SAKO, K. & FUKAGAWA, R. 2007. Numerical simulation of soil–water interaction using smoothed particle hydrodynamics (SPH) method. *Journal of Terramechanics,* 44**,** 339-346.

CABRERA, M. & ESTRADA, N. 2019. Granular column collapse: Analysis of grain-size effects. *Phys Rev E,* 99**,** 012905.

CABRERA, M. & ESTRADA, N. 2021. Is the Grain Size Distribution a Key Parameter for Explaining the Long Runout of Granular Avalanches? *Journal of Geophysical Research: Solid Earth,* 126.

CABRERA, M. A., LEONARDI, A. & PENG, C. 2020. Granular flow simulation in a centrifugal acceleration field. *Géotechnique,* 70**,** 894-905.

CABRERA, M. A. & WU, W. 2017. Experimental modelling of free-surface dry granular flows under a centrifugal acceleration field. *Granular Matter,* 19.

CAGNOLI, B. & PIERSANTI, A. 2015. Grain size and flow volume effects on granular flow mobility in numerical simulations: 3‐D discrete element modeling of flows of angular rock fragments. *Journal of Geophysical Research: Solid Earth,* 120**,** 2350-2366.

CHEN, W. & QIU, T. 2012. Numerical Simulations for Large Deformation of Granular Materials Using Smoothed Particle Hydrodynamics Method. *International Journal of Geomechanics,* 12**,** 127-135.

CROSTA, G. B., IMPOSIMATO, S. & RODDEMAN, D. 2009. Numerical modeling of 2-D granular step collapse on erodible and nonerodible surface. *Journal of Geophysical Research,* 114.

DORBOLO, S., MAQUET, L., BRANDENBOURGER, M., LUDEWIG, F., LUMAY, G., CAPS, H., VANDEWALLE, N., RONDIA, S., MÉLARD, M., VAN LOON, J., DOWSON, A. & VINCENT-BONNIEU, S. 2013. Influence of the gravity on the discharge of a silo. *Granular Matter,* 15, 263-273.

FÁVERO, N., ALOMIR H. & BORJA, R. I. 2018. Continuum hydrodynamics of dry granular flows employing multiplicative elastoplasticity. *Acta Geotechnica,* 13, 1027-1040.

FERN, E. J. & SOGA, K. 2016. The role of constitutive models in MPM simulations of granular column collapses. *Acta Geotechnica,* 11, 659-678.

GUE., C. S., BOLTON., K. S. M. & THUSYANTHAN., N. I. 2010. Centrifuge modelling of submarine landslide flows. *In: Physical Modelling in Geotechnics-Proceedings of the 7th International Conference on Physical Modelling in Geotechnics, ICPMG 2010,* 2, 1113-1118.

HOANG, U. T. & NGUYEN, N. H. T. 2023. Particle shape effects on granular column collapse using superquadric DEM. *Powder Technology,* 424.

J.J.MONAGHAN 1994. Simulating Free Surface Flows with SPH. *Journal of Computational Physics,* 110, 399-406.

JING, L., KWOK, C. Y., LEUNG, Y. F., ZHANG, Z. & DAI, L. 2018a. Runout Scaling and Deposit Morphology of Rapid Mudflows. *Journal of Geophysical Research: Earth Surface,* 123, 2004-2023.

JING, L., YANG, G. C., KWOK, C. Y. & SOBRAL, Y. D. 2018b. Dynamics and scaling laws of underwater granular collapse with varying aspect ratios. *Physical Review E,* 98.

KERMANI, E. & QIU, T. 2018. Simulation of quasi-static axisymmetric collapse of granular columns using smoothed particle hydrodynamics and discrete element methods. *Acta Geotechnica,* 15, 423-437.

KLEINHANS, M. G., MARKIES, H., DE VET, S. J., IN 'T VELD, A. C. & POSTEMA, F. N. 2011. Static and dynamic angles of repose in loose granular materials under reduced gravity. *Journal of Geophysical Research,* 116.

LAI, Z., JIANG, E., ZHAO, L., WANG, Z., WANG, Y. & LI, J. 2023. Granular column collapse: Analysis of inter-particle friction effects. *Powder Technology,* 415.

LAI, Z., VALLEJO, L. E., ZHOU, W., MA, G., ESPITIA, J. M., CAICEDO, B. & CHANG, X. 2017. Collapse of Granular Columns With Fractal Particle Size Distribution: Implications for Understanding the Role of Small Particles in Granular Flows. *Geophysical Research Letters,* 44.

LAJEUNESSE, E., MANGENEY-CASTELNAU, A. & VILOTTE, J. P. 2004. Spreading of a granular mass on a horizontal plane. *Physics of Fluids,* 16, 2371-2381.

LAJEUNESSE, E., MONNIER, J. B. & HOMSY, G. M. 2005. Granular slumping on a horizontal surface. *Physics of Fluids,* 17, 103302.

LAJEUNESSE, E., QUANTIN, C., ALLEMAND, P. & DELACOURT, C. 2006. New insights on the runout of large landslides in the Valles‐Marineris canyons, Mars. *Geophysical Research Letters,* 33.

LI, Y., WEI, D., ZHANG, N. & FUENTES, R. 2024. Effect of basal friction on granular column collapse. *Granular Matter,* 26.

LUBE, G., HUPPERT, H. E., SPARKS, R. S. J. & HALLWORTH, M. A. 2004. Axisymmetric collapses of granular columns. *Journal of Fluid Mechanics,* 508, 175-199.

LUCAS, A., MANGENEY, A. & AMPUERO, J. P. 2014. Frictional velocity-weakening in landslides on Earth and on other planetary bodies. *Nat Commun,* 5**,** 3417.

LUCAS, A., MANGENEY, A., MÈGE, D. & BOUCHUT, F. 2011. Influence of the scar geometry on landslide dynamics and deposits: Application to Martian landslides. *Journal of Geophysical Research,* 116.

MAN, T., HUPPERT, H. E., LI, L. & GALINDO-TORRES, S. A. 2021a. Deposition morphology of granular column collapses. *Granular Matter,* 23.

MAN, T., HUPPERT, H. E., LI, L. & GALINDO-TORRES, S. A. 2021b. Finite-Size Analysis of the Collapse of Dry Granular Columns. *Geophysical Research Letters,* 48.

MANGENEY, A., ROCHE, O., HUNGR, O., MANGOLD, N., FACCANONI, G. & LUCAS, A. 2010. Erosion and mobility in granular collapse over sloping beds. *Journal of Geophysical Research,* 115.

MARSHALL, J. P., HURLEY, R. C., ARTHUR, D., VLAHINIC, I., SENATORE, C., IAGNEMMA, K., TREASE, B. & ANDRADE, J. E. 2018. Failures in sand in reduced gravity environments. *Journal of the Mechanics and Physics of Solids,* 113**,** 1-12.

MERUANE, C., TAMBURRINO, A. & ROCHE, O. 2010. On the role of the ambient fluid on gravitational granular flow dynamics. *Journal of Fluid Mechanics,* 648**,** 381-404.

MONAGHAN & GINGOLD, R. A. 1983. Shock Simulation by the Particle Method of SPH. *Journal of Computational Physics,* 52**,** 374-389.

NAKASHIMA, H., SHIOJI, Y., KOBAYASHI, T., AOKI, S., SHIMIZU, H., MIYASAKA, J. & OHDOI, K. 2011. Determining the angle of repose of sand under low-gravity conditions using discrete element method. *Journal of Terramechanics,* 48**,** 17-26.

P. G. HOFMEISTER, J. B. A. D. H. 2009. The Flow Of Granular Matter Under Reduced-Gravity Conditions. *AIP Conference Proceedings,* 1145.

POLANÍA, O., CABRERA, M., RENOUF, M. & AZÉMA, E. 2022. Collapse of dry and immersed polydisperse granular columns: A unified runout description. *Physical Review Fluids,* 7**,** 084304.

ROCHE, O., ATTALI, M., MANGENEY, A. & LUCAS, A. 2011. On the run-out distance of geophysical gravitational flows: Insight from fluidized granular collapse experiments. *Earth and Planetary Science Letters,* 311**,** 375-385.

SHEIKH, B., QIU, T. & AHMADIPUR, A. 2021. Comparison of SPH boundary approaches in simulating frictional soil–structure interaction. *Acta Geotechnica,* 16**,** 2389-2408.

STROM, A., LI, L. & LAN, H. 2019. Rock avalanche mobility: optimal characterization and the effects of confinement. *Landslides,* 16**,** 1437-1452.

SU, D., ZHANG, R., LEI, G. & LI, Q. 2022. Experimental and numerical study on collapse of quasi-two-dimensional bilayer granular column. *Advanced Powder Technology,* 33.

SZEWC, K. 2017. Smoothed particle hydrodynamics modeling of granular column collapse. *Granular Matter*, 19.

TAPIA-MCCLUNG, H. & ZENIT, R. 2012. Computer simulations of the collapse of columns formed by elongated grains. *Phys Rev E Stat Nonlin Soft Matter Phys,* 85**,** 061304.

TENG MAN, H. E. H. 2022. Man Teng Influence of Cross-section Shape on Granular Column. *Powder Technology*.

THOMPSON, E. L. & HUPPERT, H. E. 2007. Granular column collapses: further experimental results. *Journal of Fluid Mechanics,* 575**,** 177-186.

VONNEUMANN, J. & RICHTMYER, R. D. 1950. A Method for the Numerical Calculation of Hydrodynamic Shocks. *Journal of Applied Physics,* 21**,** 232-237.

WARNETT, J. M., DENISSENKO, P., THOMAS, P. J., KIRACI, E. & WILLIAMS, M. A. 2014. Scalings of axisymmetric granular column collapse. *Granular Matter,* 16**,** 115-124.

WEI, D., WANG, J., NIE, J. & ZHOU, B. 2018. Generation of realistic sand particles with fractal nature using an improved spherical harmonic analysis. *Computers and Geotechnics,* 104**,** 1-12.

YANG, E., BUI, H. H., DE STERCK, H., NGUYEN, G. D. & BOUAZZA, A. 2020. A scalable parallel computing SPH framework for predictions of geophysical granular flows. *Computers and Geotechnics,* 121.

ZHANG, R., SU, D., LEI, G. & CHEN, X. 2021. Three-dimensional granular column collapse: Impact of column thickness. *Powder Technology,* 389**,** 328-338.

ZHU, R., HE, Z., ZHAO, K., VOWINCKEL, B. & MEIBURG, E. 2022. Grain-resolving simulations of submerged cohesive granular collapse. *Journal of Fluid Mechanics,* 942.